Crystal Defects and Optical Emissions of Pulse Electrodeposited ZnO Films

Cristina V. Manzano[1,*], Aida Serrano[2], Álvaro Muñoz-Noval[3], José F. Fernandez[2] and Marisol Martín-González[1,*]

[1]Instituto de Micro y Nanotecnología, IMN-CNM, CSIC (CEI UAM + CSIC), Isaac Newton 8, E-28760, Tres Cantos, Madrid, Spain
[2]Departamento de Electrocerámica, Instituto de Cerámica y Vidrio, CSIC, Kelsen 5, E-28049, Madrid, Spain
[3]Departamento de Física de Materiales, Universidad Complutense de Madrid, Ciudad Universitaria s/n, E-28040, Madrid, Spain

Abstract

ZnO has been widely studied in the last decades as an n-type semiconductor due to its wide application range, for example, in optoelectronics, solar cells, light-emitting diodes, thermoelectrics, amongst others. The material efficiency for certain applications is highly dependent on the presenting film morphology. Electrodeposition is well-known as a technique with precise control over the structural and morphological properties of the obtained materials. When the structural and morphological properties are tuned, it is possible to find a wide variety of defects in the ZnO structure. In this study, ZnO films were grown using pulsed electrodeposition with variation of the reduction potential. The crystal order, structural defects and optical emissions of the films have been analyzed by X-Ray Diffraction (XRD), X-ray Absorption Near-Edge Structure (XANES) and Extended X-ray Absorption Fine Structure (EXAFS) and Photoluminescence (PL). ZnO film grown at less negative reduction potential presents a stronger texture along [0001] by XRD, higher crystalline order, and more zinc vacancies by XANES and EXAFS. The films obtained at less negative potential present less OH^- trapped in the ZnO structure and a relatively higher level of defects O_i^0, O_{Zn}^0, $O_i^{-/2-}$ and $O_{Zn}^{0/-}$ than those grown at higher reduction potentials by PL. This will be related to the fact that at less negative potentials there is less concentration of OH^- at the film surface than at more negative potentials. The combination of X-ray absorption spectroscopy and photoluminescence reveals the complicated nature of the atomic defect in electrodeposited ZnO films. Allowing to evidence the preferential presence of atomic defect as a function of the reduction

potential. In this work, we have also compared those defects with reference compounds such as a Zn foil and ZnO polycrystalline powder.

Keywords: electrodeposition, ZnO, reduction potential, XAS, Photoluminescence

1. Introduction

ZnO is an n-type semiconductor, presenting a hexagonal structure, high electron mobility, a direct wide bandgap of 3.36 eV, large excitation energy of 60 meV at room temperature, while also exhibiting an efficient emission in the ultraviolet and visible ranges. ZnO has been extensively studied due to the wide application range which the materials can be employed for optoelectronics [1], light-emitting diodes [2], batteries [3], sensors [4], sensitized solar cells [5], and thermoelectrics [6]. These applications are different depending on the ZnO morphology, among other material characteristics (or structural properties). Also, the fact of obtaining different morphologies and structural properties implies different intrinsic defects (zinc and oxygen vacancies and interstitial sites) in this material. These different defects can alter physical properties such as the grain boundary, the electronic and optical properties of ZnO [7]. Interstitial zinc atoms contribute to the electrical conductivity [8, 9], depending on the values of the electrical conductivity the application of ZnO is different, can be used, for example, for batteries or solar cells. Another application is for sensing, the sensing process to the chemical environment is controlled by oxygen vacancies that influence the electronic properties and the optical response. Depending on the sensing molecule, the electrical conductivity is higher or smaller [7].”

ZnO films can be fabricated through several different physical growth methods, such as RF magnetron sputtering [10], pulsed laser deposition [11], or chemical growth techniques as chemical bath deposition [12], dry dispersion process [13, 14], or DC electrodeposition [15]. One of the most interesting routes to control the morphological and structural features of ZnO films is electrodeposition. This technique allows the growth at room temperature, fast deposition rates, and excellent control over the crystallographic structure and morphology. Besides, it is a low-cost method and scalable to industry requirements. It is known that by pulsed electrodeposition different

morphologies of ZnO (hexagonal columns, hexagonal platelets, needles, or planar growth) are favored depending on the applied reduction potential [16]. The mechanism behind these morphologies changes is ascribed to the concentration of OH^- generated by reaction (1), the local pH at the electrode surface, to the Faradaic efficiency of the process for each electrodeposition conditions, and the amount of Zn^{2+} available [16]. According to the general reactions:

$$NO_3^- + H_2O + 2e^- \rightarrow NO_2^- + 2OH^- \quad (1)$$

$$Zn^{2+} + 2OH^- \rightarrow Zn(OH)_2 \rightarrow ZnO + H_2O \quad (2)$$

Consequently, the growth rate and morphology of the films prepared by electrodeposition can be controlled by the growth conditions. However, the fact that different morphologies can be obtained by the different electrodeposition conditions must imply that different defects and mechanisms are involved during growth. These defects can be investigated using several techniques. Specifically, a study combining X-ray Absorption Near-Edge Structure (XANES) and Extended X-ray Absorption Fine Structure (EXAFS) measurements are useful to analyze the oxidation state and the local structure (first neighbors) around the Zn absorbing atoms [17]. This structural information can help to understand the global defects observed using Photoluminescence (PL). PL emission provides data on the deep and shallow energy levels for different vacancies or interstitials inside the ZnO structure. To date, studies in which the defects of ZnO are analyzed combining X-ray Absorption Spectroscopy (XAS) and PL techniques are limited in literature [17, 18]; even-though these characterization techniques are complementary and allow a semi-quantitative analysis of the defects in ZnO. To understand the influence of the electrodeposition conditions and the local pH to improve the final properties of the ZnO, it is important to characterize the defects found in ZnO films and relate these to the morphology and growth conditions. The novelty of this work is based on the combination of both techniques (XAS and PL) to reveal the complex nature of crystal defect in ZnO films grown by electrodeposition.

The aim of this study is therefore to analyze the defects of different ZnO morphologies grown by pulsed electrodeposition through XAS and PL measurements as a function of the reduction potential. First, the crystallographic structure and morphology of the ZnO films are analyzed by X-Ray Diffraction (XRD) and Scanning Electron

Microscopy (SEM), respectively. From XRD measurements, the Harris texture coefficient was calculated to quantify the degree of preferred orientation of the films. A deep study of ZnO film defects based on the reduction potential is performed here using both XANES and EXAFS measurements. This work opens a new line to investigate the defects found in ZnO films grown using electrochemical techniques, from which it is possible to have control over the morphologies found in these films.

2. Experimental methods

2.1. Fabrication of the ZnO films

The electrodeposition of ZnO films was performed in 0.1 M $Zn(NO_3)_2$ aqueous solution at 80 ± 1 ºC in similar conditions to previous studies [16, 19, 20]. The growth was carried out in a conventional electrochemical cell of three electrodes: a platinum mesh, Ag/AgCl, and 150 nm Au/5 nm Cr/Si were used as a counter electrode, reference electrode, and working electrode, respectively. The cell was controlled with an Autolab 302.0 bi-potentiostat. ZnO films were electrodeposited using pulsed deposition between a reduction potential and oxidation potential to obtain different concentrations of OH^- respect to Zn^{2+}. The reduction potential was changed, -1.5 V, -1.3 V, -0.9 V, and -0.6 V for 2 s, while the oxidation potential was fixed to +0.9 V for 1 s, in all the cases. The total cycle number was 1800 for all the films.

2.2. Films characterization

The crystallographic structure of the film was analyzed using XRD with a Philips X-Pert Cuα X-Ray transmitter four circle diffractometer. The morphological characterization was obtained using a Hitachi S-800 Scanning Electron Microscopy (SEM) with a 25 kV accelerating voltage. To investigate the oxidation state and the local structure effects induced by the different reduction potential during the electrodeposition of the films, X-Ray Absorption Spectroscopy (XAS) experiments were performed. Both X-Ray Absorption Near-Edge Structure (XANES) and Extended X-ray Absorption Fine Structure (EXAFS) measurements were carried out at the Spanish CGR beamline BM25-SpLine at The ESRF- The European Synchrotron, Grenoble (France). The beamline monochromator is a pseudo-channel-cut type with two Si(111) crystals refrigerated at 200 K by a homemade ethanol cooling system. XAS spectra of films were collected at the Zn

K-edge (9659 eV) at room temperature in fluorescence mode using a 13-elements Si(Li) detector. The reference ZnO polycrystalline micrometric powder, from Asturiana de Cinc S.A. (Spain), and the Zn foil were measured in transmission detection configuration using two ionization chambers. The XAS data were analyzed with a standard procedure using Athena and Artemis software [21]. Photoluminescence (PL) measurements were performed to analyze the defects of ZnO films. The films were excited with a pulsed Nd:YAG tripled laser (355 nm wavelength, 15 ns pulse, 20 kHz repetition rate) modulated in intensity with an optical modulator (177 Hz). The light emitted in the ultraviolet and/or visible range was filtered by suitable long-pass filters and dispersed by a monochromator with a 300 mm focal length (diffraction grating: 1200 lines/mm) and detected through a cooled photomultiplier, connected to a lock-in amplifier.

3. Results and discussion

3.1. Structural and morphological characterization of ZnO films

The crystallographic structure of the ZnO films grown at different reduction potential was studied using XRD, whose patterns are shown in Fig. 1A. All the films present (002) as maximum diffraction peak, indicating that the films are strongly oriented along [0001] direction with the *c-axis* perpendicular to the substrate.

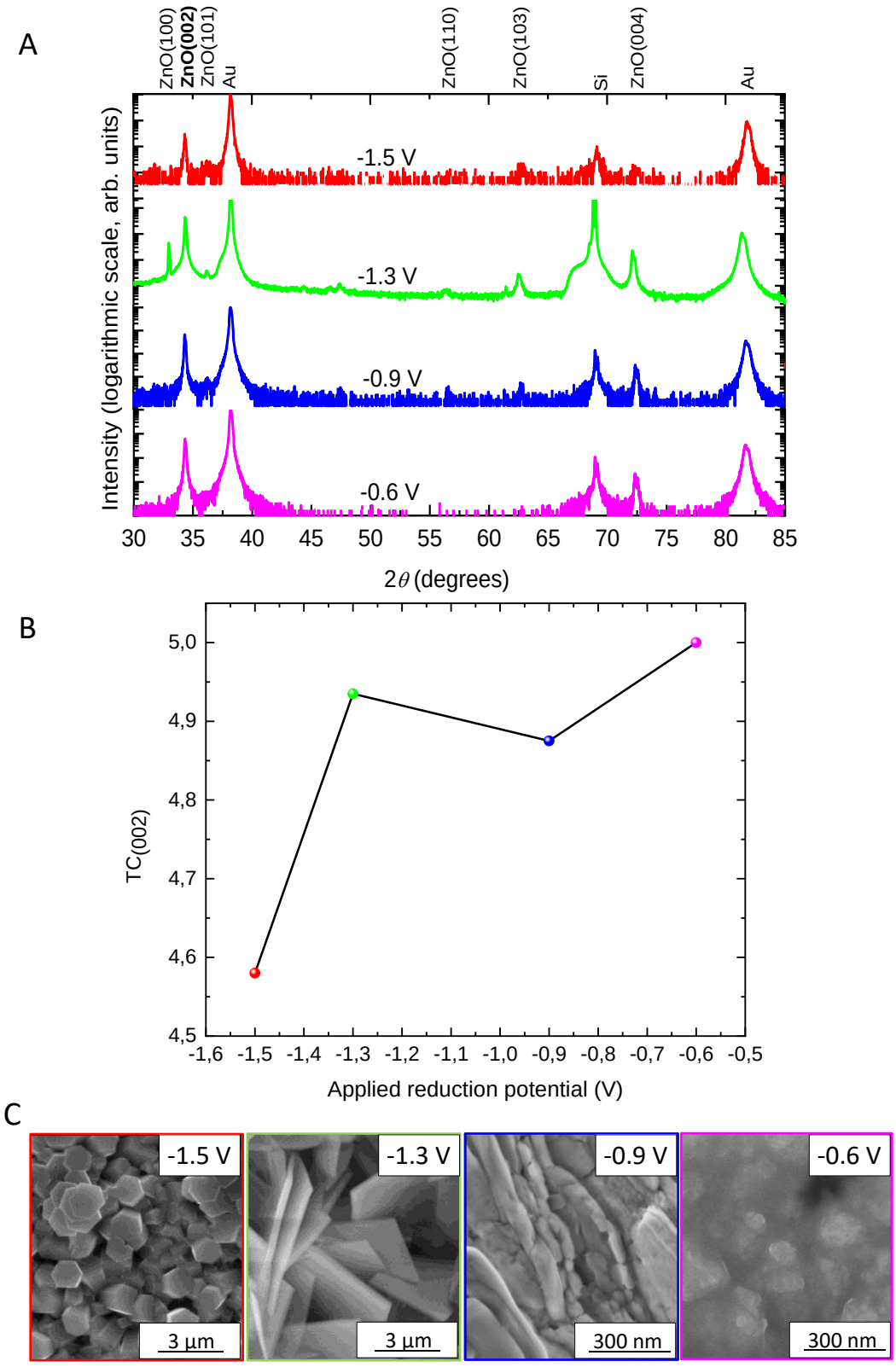

Fig. 1 (A) X-ray diffractograms of the different ZnO films on the logarithmic scale. (B) Texture coefficient (TC) as a function of the reduction potential of ZnO films. (C) SEM images of the surface morphology for the different ZnO films. The color around the SEM pictures corresponds to the color in XRD.

Harris's texture analysis [22] was performed to quantitatively obtain a degree of preferred orientation. The equation of the texture coefficient is:

$$TC_{(hkl)} = \frac{\frac{I_{(hkl)}}{I^0_{(hkl)}}}{\frac{1}{N}\sum\frac{I_{(hkl)}}{I^0_{(hkl)}}} \quad (1)$$

where: $I_{(hkl)}$ and $I^0_{(hkl)}$ – is the intensity of a generic peak observed in the experimental XRD and the literature value from the database (JCPDS 76-0704), respectively, and N – number of reflections considered in the analysis. In this case, the number of reflections used for the calculation of the texture coefficients were five corresponding to the following diffraction peaks: (100), (002), (101), (110), and (103); see supporting information.

The standard deviation (σ) indicates the deviation intensity of the experimental XRD from published values of JCPDS and is calculated as:

$$\sigma = \sqrt{\frac{\sum\left(TC_{(hkl)} - 1\right)^2}{N}} \quad (2)$$

The values of the texture coefficient and its standard deviation are shown in Table 1 and the texture coefficient along crystallographic direction [0001] for the different films is shown in Fig. 1B. The values of the texture coefficient along the [0001] direction are 3.99, 4.91, 4.88, and 5.00 for -1.5 V, -1.3 V, -0.9 V, and -0.6 V, respectively. The texture coefficient is higher for the film grown at the less negative reduction potential (-0.6 V); while the lower value is obtained for the films deposited at more negative potential (-1.5 V). In conclusion, the film which presents a higher texture along [0001] direction is the one grown at -0.6 V.

Table 1. Harris texture coefficient, standard deviation, FWHM of (002) diffraction peak, and crystalline size for the different ZnO films obtained from the XRD measurements.

Reduction potential	Intensity XRD	Intensity JCPDS	Texture coefficient ($TC_{(002)}$)	Standard deviation (σ)	FWHM (002)	Crystallite size (nm)
-1.5 V	84	415	3.99	1.49	0.13	62.7
-1.3 V	4461	415	4.91	1.95	0.15	57.1
-0.9 V	2416	415	4.88	1.94	0.14	61.8
-0.6 V	3428	415	5.00	2.00	0.15	55.4

To determine the crystallite size in the (002) diffraction peak was calculated using the Debye-Scherer equation:

$$D = \frac{0.9 \cdot \lambda}{\beta \cdot cos\theta} \quad (3)$$

where: D – crystallite size, λ – radiation wavelength, β – broadening of Full-Width-Half-Maximum (FWHM) of the intense peak and θ – Bragg angle. As is shown in table 1, the crystallite size was found to be 55.4, 61.8, 57.1, and 62.7 nm for -0.6 V, -0.9 V, -1.3 V, and -1.5 V, respectively, and any trend is identified.

Fig. 1C shows the scanning electron microscopy images of the different ZnO films. The films morphology changes depending on the reduction potential applied during the electrodeposition. In agreement with a previous study [16], different morphologies were identified depending on the reduction potential: hexagonal columns, hexagonal platelets, flowers, and 2D growth for -1.5 V, -1.3 V, -0.9 V and -0.6 V, respectively. The origin of these different morphologies was related to the OH^-/Zn^{2+} ratio, the local pH at the electrode surface, and the Faradaic efficiency of the process for each potential [12]. For this reason and considering the different morphological characteristics and texture coefficients of the films, the defect structure of ZnO is expected to be different according to the differences in crystal growth. Therefore, a deep local structural analysis and defects characterization of ZnO films grown under these specific electrodeposition conditions are followed in detail.

3.2. XANES and EXAFS characterization of ZnO films

Fig. 2 shows the XANES results obtained for ZnO films depending on the growth conditions, which implies the applied reduction potential, in this case. XANES measurements of ZnO polycrystalline powder and Zn foil references are presented for comparison. Fig. 2A shows the Zn K-absorption edge for XANES spectra of films where the peaks named as A, B, and C can be differentiated correspondingly to electron transitions from the occupied Zn-1s to unoccupied Zn-4p states along the axes of the ZnO unit cell [23], following a similar absorption signal than the ZnO standard. From the main characteristics of these main peaks, several works have analyzed the effect of different Zn and O vacancy positions [23-25]. In our case, a decrease of the intensity in the peak B as the applied reduction potential is more negative during the growth of ZnO films is identified, which may indicate a reduction of the concentration of Zn vacancies, V_{Zn}. Zinc vacancies are acceptor native defects of the ZnO structure that can exist in neutral, V_{Zn}^{x}, singly ionized, $V_{Zn}^{\prime}$, or doubly ionized forms, $V_{Zn}^{\prime\prime}$. In equilibrium, the chemical balance between the concentration of such vacancies is maintained [26]. However, the predominant n-type nature of the ZnO structure is governed by the presence of oxygen

vacancies. As can be observed in Fig.2A, the ZnO film electrodeposited at -0.6 V presents more zinc vacancies than the film grown at -0.9 V, and that one more than the film obtained at -1.3 V. Being the film grown at -1.5 V the one with less concentration of zinc vacancies. Concerning the peak A and C, not significant variations are noted. Besides, changes in the energy position at the absorption edge of XANES spectra are also identified. Specifically, the ZnO polycrystalline powder reference with an oxidation state of 2+ shows a shift towards larger energy values for the Zn foil with a valence of 0 (at absorption edge energy of 9659 eV), a similar trend to other transition metals [27, 28]. From the linear relationship between the absorption edge and the valence, it is possible to estimate the average oxidation state in each film. As Fig. 2B shows, at the more negative reduction potential (-1.5 V) the films present a lower average oxidation state (lower energy value at the absorption edge) towards the position of Zn foil. The films prepared at -0.9 and -1.3 V presents very close values of energy at the Zn absorption edge to that of the ZnO polycrystalline powder reference. For the specific case of ZnO film fabricated at the less negative reduction potential (-0.6 V), a larger average oxidation state is identified with the absorption edge position falling at larger energy values than the ZnO reference.

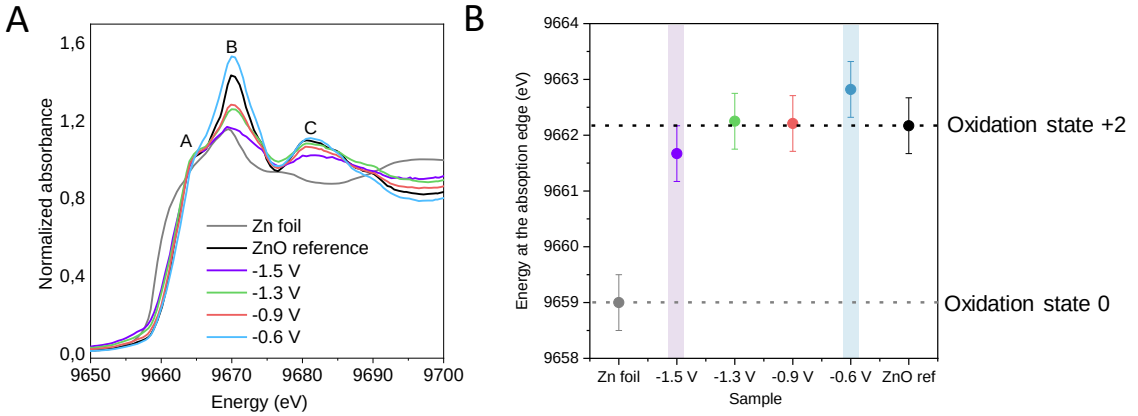

Fig. 2 (A) XANES spectra at the Zn K-absorption edge and (B) energy at the absorption edge of ZnO films grown at different reduction potential. XANES results of ZnO polycrystalline powder and Zn foil reference are also presented, indicating the oxidation state in each case.

In conclusion, ZnO film grown at the more negative reduction potential (-1.5 V) exhibits less oxidation state than the films electrodeposited at the less negative reduction potential. The Zn is +2 for the films grown at -1.3 V and -0.9 V. While, the oxidation state of the Zn is higher than 2 for the film grown at -0.6 V. This conclusion is in agreement to the results obtained from the peak B of XANES spectra, where the ZnO

films grown at the less negative reduction potential (-0.6 V) present more zinc vacancies concentration, a deficit of Zn in the ZnO structure, than the films electrodeposited at the more negative reduction potential (-1.5 V).

The applied reduction potential conditions of ZnO films may also modify the vacancy concentration during the growth process, altering the local structure. To evaluate the first neighbors, EXAFS measurements were performed on the ZnO films at the Zn K-edge. Fig. 3A shows the EXAFS signal in the k-space for the different films prepared in the interval from 2.5 to 10.5 $Å^{-1}$ with a k weight of 2, which were taken using the FEFF software [21, 29] and ZnO reference [30]. Slight variations in the intensity of oscillations are identified while phase modifications are not noted, suggesting a similar overall structure between the films.

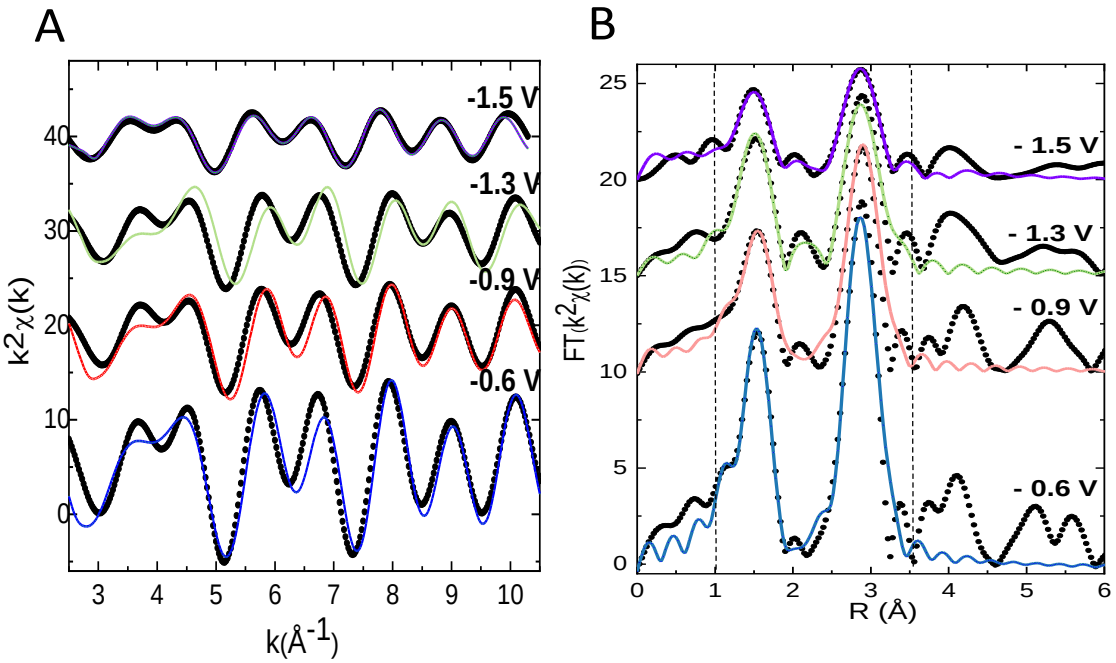

Fig. 3(A) $k^2 \cdot \chi(k)$ EXAFS spectra and (B) FT modulus of the EXAFS signal at Zn K-edge for the different ZnO films. The black dots represent the experimental data, and the color continuous lines show the best fitting simulations of the first and second peaks.

The back Fourier Transform (FT) of the oscillations gives the radial distribution function of the local structure of the films within a reasonable compromise of signal to noise ratio. As Fig. 3B displays, finding the best EXAFS fitting for the ZnO films grown at -1.5 V. The radial distribution functions have been fitted within the real space interval between 1 and 3.6 Å (R range marked on Fig. 3B). The adjustment has been done by considering a three-shell model with one first shell of O atoms (Zn-O), and two-second

shells composed by Zn atoms (Zn-Zn(1) and Zn-Zn(2)), based on a hexagonal ZnO reference [30]. This three-shell model considers one shell of O neighbors at circa 1.98 Å from the scattering atom (Zn), and two-second shells composed by Zn atoms, at distances around 3.21 and 3.25 Å. The fitting, fixing the E_0 (shift of edge energy) to 5 eV, gave the rest of EXAFS parameter values: R (bond length), N (mean number of neighbors) and DW (Debye-Waller) factor, σ^2, which are summarized in Table 2 for all ZnO films and ZnO polycrystalline powder references for their corresponding modeled shells.

Table 2. Fits parameters from EXAFS analysis (interatomic distance, R, the coordination number of neighbors, N(Zn) and N(O), and Debye-Waller (DW) factor, σ^2) of first Zn-O and Zn-Zn distances for the ZnO films and ZnO polycrystalline powder.

	Shell	**Interatomic distance, R (Å)**	**Coordination number, N**	**Debye-Waller factor, σ^2 ($Å^2$)**
ZnO polycrystalline powder	Zn-O	1.98 (1)	4.0 (8)	5.5 (7) $\cdot 10^{-3}$
	Zn-Zn(1)	3.22 (2)	6.0 (9)	11.5 (7)$\cdot 10^{-3}$
	Zn-Zn(2)	3.26 (4)		
- 1.5 V	Zn-O	1.98 (1)	1.8 (4)	6.3 (7)$\cdot 10^{-3}$
	Zn-Zn(1)	3.21 (2)	2.4 (5)	12.3 (7)$\cdot 10^{-3}$
	Zn-Zn(2)	3.25 (3)		
- 1.3 V	Zn-O	1.98 (1)	2.6 (6)	3.6 (5)$\cdot 10^{-3}$
	Zn-Zn(1)	3.21 (2)	5.1 (9)	15.5 (5)$\cdot 10^{-3}$
	Zn-Zn(2)	3.25 (2)		
- 0.9 V	Zn-O	1.98 (1)	3.1 (7)	4.7 (5) $\cdot 10^{-3}$
	Zn-Zn(1)	3.22 (2)	3.7 (7)	10.2 (5) $\cdot 10^{-3}$
	Zn-Zn(2)	3.26 (4)		
- 0.6 V	Zn-O	1.98(1)	4.6 (9)	4.0 (7)$\cdot 10^{-3}$
	Zn-Zn(1)	3.22 (2)	6.4 (3)	10.7 (7)$\cdot 10^{-3}$
	Zn-Zn(2)	3.26 (4)		

Fig. 4 shows the coordination numbers of first neighbors, N(O) and N(Zn), and the DW factors, σ^2(Zn-O) and σ^2(Zn-Zn), obtained from the EXAFS fittings of two first peaks for the ZnO films as a function of the reduction potential. As Fig. 4A presents, a decrease of the coordination numbers, both N(O) and N(Zn), is obtained as the reduction potential decreases (is more negative), except for N(Z) in the film grown at -1.3V. In this way, considering a homogeneous distribution of O atoms along the lattice, the oxygen

deficiency in the structures as a function of the reduction potential is semi-quantified by obtaining the number of neighbors. Results agree with the average oxidation state of ZnO films obtained from the XANES measurement (see Fig. 2). Specifically, for the films grown at -0.6 V, the coordination number is greater than for the ZnO polycrystalline powder reference as Table 2 indicates, which can be corroborated with the highest crystallinity of the films measured by XRD.

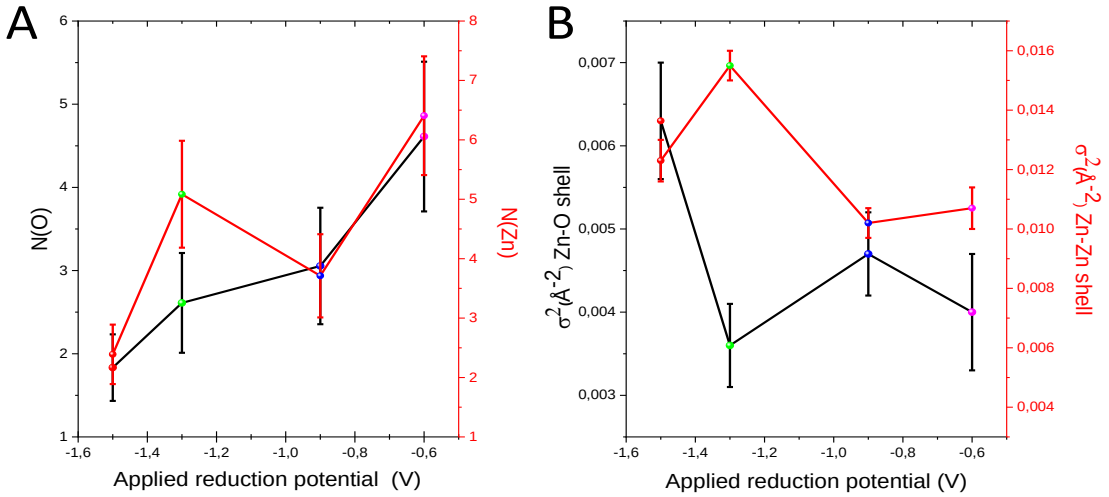

Fig. 4. (A) Coordination number, N(Zn) and N(O) and (B) Debye-Waller factor, σ^2 (Zn-O), and σ^2(Zn-Zn), for ZnO films grown at different reduction potentials.

DW factors for the first and second shell, Zn-O and Zn-Zn layers, of the different ZnO films, are shown in Fig. 4B. On average, this factor is lower for the Zn-O than the Zn-Zn shells. Comparing both DW factors the film with the lowest values, on balancing and considering the errors of the DW factors, are the films grown at a more negative potential, -0.6 V. This indicates that these films exhibit the greater structural order. Out of this trend is the film grown at -1.3 V, both in the coordination values and the DW parameters calculated. Table 3 shows the lattice parameters (*c* and *a*) and the ratio *c/a* of the ZnO structure for each ZnO film, obtained according to the model of reference [2]. These crystallographic parameters are calculated from the bond length distances Zn-O and Zn-Zn to be similar for all the ZnO films independently on growth conditions.

Table 3. Lattice parameters (*a*, *c*, *u*, and *c/a*) obtained from the Zn-O and Zn-Zn distances of EXAFS results for the different ZnO films and polycrystalline powder.

	***a* (Å)**	***c* (Å)**	***U***	***c/a***
ZnO polycrystalline powder	3.26 (1)	5.23 (1)	0.38 (2)	1.60 (4)
- 1.5 V	3.25 (1)	5.21 (7)	0.38 (7)	1.60 (1)
- 1.3 V	3.25 (1)	5.21 (5)	0.38 (6)	1.60 (1)
- 0.9 V	3.26 (1)	5.23 (4)	0.38 (6)	1.60 (1)
- 0.6 V	3.26 (1)	5.23 (6)	0.38 (7)	1.60 (1)

In conclusion, the ZnO films grown at the less negative reduction potential (-0.6 V) exhibits more zinc vacancies concentration and more average oxidation state than the films obtained at the more negative reduction potential, being the other extreme the films grown at -1.5 V. Moreover, a greater coordination number and a lower crystalline disorder, in both Zn-O and Zn-Zn shells, in the ZnO structure for the film prepared at -0.6 V was identified. These results can be related to the crystallographic structure of the studied films, indicating a greater structural order for the films with larger textured coefficient along [0001] direction, which means in the ZnO films grown at -0.6 V.

3.3. Photoluminescence of ZnO films

The structural changes identified in the ZnO films depending on reduction potentials can be affected by the defects incorporated into the structure during the growth process. Therefore, the intrinsic defects of electrodeposited ZnO films under different reduction potentials were analysed using PL measurements. Fig. 5A and 5B show the PL intensity as a function of wavelength and the relative weight of the different emissions, respectively, as a function of applied reduction potential in the visible range.

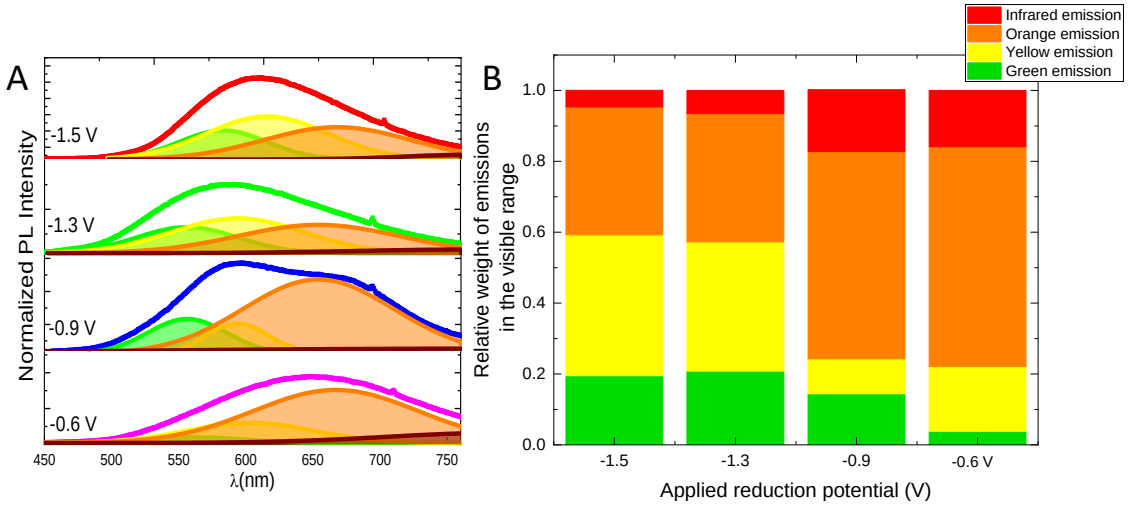

Fig 5. (A) Photoluminescence and Gaussian deconvolution of emission and (B) the relative weight of the different emissions in the visible range for the ZnO films obtained at different applied reduction potentials. The total area is normalized to the unit.

To describe the different emissions in the visible range of the ZnO films the PL emission was deconvoluted in four emissions using a Gaussian function according to a PL model previously proposed [19]. These four emissions are *green*, *yellow*, *orange-red*, and *infrared* emission. G*reen* and *yellow* emissions are due to a transition from the donor OH^- to the acceptor zinc vacancies and to interstitial oxygen (O_i^0), respectively. O*range-red* emission is probably due to transitions from the conducting band to O_i^- and O_{Zn}^0 defects and the *infrared emission* to transition from $O_i^{-/2-}$ and $O_{Zn}^{0/-}$ defects to the valence band. To quantify the different contributions, the relative weight of the different emissions in the visible range as a function of reduction potential was calculated (see Fig. 5B). From the PL measurements, it can be concluded that green and yellow emissions are higher in the films deposited at the more negative reduction potential (-1.5 V and -1.3 V) than in the films grown at the less negative reduction potential (-0.9 V and -0.6 V). Due to both emissions are due to transitions from OH^- to the acceptor zinc vacancies for *green* emission or interstitial oxygen (O_i^0) for *yellow* emission, the films obtained at a less negative potential (-0.9 V and -0.6 V) present less OH^- trapped in the ZnO structure. This conclusion fits very well with the conclusion extracted from the pH model proposed in a previous study [16]. Consequently, considering the complementary information, it can be concluded that the film grown at less reduction potential (-0.6 V) presents less OH^- trapped in the structure (since it is also produced at lower pH) and exhibits more zinc vacancies according to XANES measurements. While the *orange-red* and *infrared emissions* are higher in the films deposited at less negative reduction potential than in the films grown at more negative reduction potential. In this case, both emissions (*orange-*

red and *infrared emissions*) are due to transitions from the conduction band to O_i^- and O_{Zn}^0 defects or from $O_i^{-/2-}$ and $O_{Zn}^{0/-}$ defects to the valance band, respectively; and then for the films grown at less negative reduction potentials (-0.9 V and -0.6 V) these kinds of defects (O_i^0, O_{Zn}^0, $O_i^{-/2-}$ and $O_{Zn}^{0/-}$) are higher than in the case of the films deposited at the more negative reduction potentials (-1.5 V and -1.3 V).

To conclude the encounters found in ZnO films analyzed by different techniques, XANES, EXAFS, and PL, are collected in Table 4.

Table 4. Summary of the findings identified in the electrodeposited ZnO films as a function of the reduction potential. The lowest and the highest values are shown in red and green, respectively, as the colour bar indicates.

Reduction potential	Crystalline order	Oxidation state	V_{Zn}	N(O) and N(Zn)	σ^2 (Zn-O)	σ^2 (Zn-Zn)	V_{Zn}	O_i^0, O_{Zn}^0, $O_i^{-/2-}$, $O_{Zn}^{0/-}$
Technique	XRD	XANES	XANES	EXAFS	EXAFS	EXAFS	PL	PL
-1.5 V		> + 2						
-1.3 V		~ + 2						
-0.9 V		~ + 2						
-0.6 V		< + 2						

The highest value *The lowest value*

Revealing the nature of the intrinsic defects is not easy, but here different experimental techniques have allowed some findings. For the ZnO films grown at -0.6V an oxygen deficiency is identified by XANES in agreement with the PL results and a lower structural disorder and a larger coordination number (EXAFS) that corroborate with a lower proportion of intrinsic defects (PL), while for the sample prepared at -1.5 V the trend is the opposite.

4. Conclusions

This study analyses the local structure and deep-level defects presenting in ZnO films grown using pulsed electrodeposition. The growth was performed between different reduction potential and fixed oxidation potential to change the ratio between OH^- and Zn^{2+} in the films. Films grown at -0.6 V presents a stronger texture along [0001] based on the extracted texture coefficient calculated from the XRD measurements. Besides, a larger average valence and a higher crystalline order in the ZnO structure was also identified for the films prepared at -0.6 V, by combining XANES and EXAFS

measurements. It is also concluded that ZnO films grown at a less negative reduction potential (-0.6 V) exhibit more zinc vacancies, V_{Zn}. The PL emission is also affected by the growth conditions, the films obtained at less negative potential (-0.9 V and -0.6 V) present less OH^- trapped in the ZnO structure than those grown at higher reduction potentials, and present a relatively higher level of defects O_i^0, O_{Zn}^0, $O_i^{-/2-}$ and $O_{Zn}^{0/-}$ than for films deposited at more negative reduction potentials (-1.5 V and -1.3 V). This work opens a new line to investigate the intrinsic defects found in ZnO films grown using electrochemical techniques by the combination of XAS and PL techniques.

AUTHOR INFORMATION

Corresponding Author:
*Email: cristina.vicente@csic.es; marisol@imm.cnm.csic.es

Notes

The authors declare no competing financial interest.

ACKNOWLEDGMENT

The authors would like to acknowledge financial support from MAT2017-86450-C4-1-R, MAT2017-86450-C4-3-R, RTI2018-095303-A-C52. C.V.M acknowledges financial support from Juan de la Cierva Incorporación grants IJCI-2017-31350. A.S. and A.M.N. acknowledge the financial support from the Comunidad de Madrid for an "Atracción de Talento Investigador" contract No. 2017-t2/IND5395 and 2018-T1/IND-10360, respectively. We acknowledge The European Synchrotron (ESRF), MICIU, and CSIC for provision of synchrotron radiation facilities in using the BM25-SpLine beamline. We also thank the BM25-SpLine staff for the technical support beyond their duties. We acknowledge the service from the MiNa Laboratory at IMN, and funding from CM (project SpaceTec, S2013/ICE2822), MINECO (project CSIC13-4E-1794) and EU (FEDER, FSE).

References

[1] K. Harun, F. Hussain, A. Purwanto, B. Sahraoui, A. Zawadzka, A.A. Mohamad, Sol–gel synthesized ZnO for optoelectronics applications: a characterization review, Materials Research Express, 4 (2017) 122001.
[2] D.-Y. Park, J.-H. Lim, M.-Y. Ha, D.-G. Moon, High Efficiency Quantum Dot Light-Emitting Diode by Solution Printing of Zinc Oxide Nanoparticles, Journal of Nanoscience and Nanotechnology, 20 (2020) 4454-4457.
[3] J. Yan, P. Xu, S. Chen, G. Wang, F. Zhang, W. Zhao, Z. Zhang, Z. Deng, M. Xu, J. Yun, Y. Zhang, Construction of highly ordered ZnO microrod@SnO2 nanowire heterojunction hybrid with a test-tube brush-like structure for high performance lithium-ion batteries: experimental and theoretical study, Electrochimica Acta, 330 (2020) 135312.
[4] S. Bai, C. Sun, T. Guo, R. Luo, Y. Lin, A. Chen, L. Sun, J. Zhang, Low temperature electrochemical deposition of nanoporous ZnO thin films as novel NO2 sensors, Electrochimica Acta, 90 (2013) 530-534.
[5] J. Cai, Z. Chen, S. Li, S. Dong, C. Wei, F. Li, Y. Peng, X. Jia, W. Zhang, A novel hierarchical ZnO-nanosheet-nanorod-structured film for quantum-dot-sensitized solar cells, Electrochimica Acta, 274 (2018) 326-333.
[6] S. Liu, Y. Piao, G. Li, M. Lan, Y. Yuan, Q. Wang, Thickness-dependent thermoelectric properties of evaporated ZnO:Al films assisted by RF atomic source, Journal of Applied Physics, 127 (2020) 055301.
[7] L. Schmidt-Mende, J.L. MacManus-Driscoll, ZnO – nanostructures, defects, and devices, Materials Today, 10 (2007) 40-48.
[8] H. Shimizu, W. Sato, Interactions of intrinsic defects formed in ZnO and their contribution to electric conductivity, Journal of Applied Physics, 126 (2019).
[9] A. Janotti, C.G. Van de Walle, Fundamentals of zinc oxide as a semiconductor, Reports on Progress in Physics, 72 (2009) 126501.
[10] A. Kabir, I. Bouanane, D. Boulainine, S. Zerkout, G. Schmerber, B. Boudjema, Photoluminescence Study of Deep Level Defects in ZnO Thin Films, Silicon, 11 (2019) 837-842.
[11] C.S. Steplecaru, M.S. Martín-González, J.F. Fernández, J.L. Costa-Krämer, How to prevent twin formation in epitaxial ZnO thin films grown on c-plane sapphire, Thin Solid Films, 518 (2010) 4630-4633.
[12] K.M. McPeak, M.A. Becker, N.G. Britton, H. Majidi, B.A. Bunker, J.B. Baxter, In Situ X-ray Absorption Near-Edge Structure Spectroscopy of ZnO Nanowire Growth During Chemical Bath Deposition, Chemistry of Materials, 22 (2010) 6162-6170.
[13] J.F. Fernández, C.V. Manzano, P. Marchet, M.S. Martín-González, J.J. Reinosa, J.J. Romero, F. Rubio-Marcos, Mechanism of Ni1?xZnxO Formation by Thermal Treatments on NiO Nanoparticles Dispersed over ZnO, (2011).
[14] F. Rubio-Marcos, C.V. Manzano, J.J. Reinosa, I. Lorite, J.J. Romero, J.F. Fernández, M.S. Martín-González, Modification of optical properties in ZnO particles by surface deposition and anchoring of NiO nanoparticles, Journal of Alloys and Compounds, 509 (2011) 2891-2896.
[15] S. Dellis, N. Pliatsikas, N. Kalfagiannis, O. Lidor-Shalev, A. Papaderakis, G. Vourlias, S. Sotiropoulos, D.C. Koutsogeorgis, Y. Mastai, P. Patsalas, Broadband luminescence in defect-engineered electrochemically produced porous Si/ZnO nanostructures, Scientific Reports, 8 (2018) 6988.

[16] C.V. Manzano, O. Caballero-Calero, S. Hormeño, M. Penedo, M. Luna, M.S. Martín-González, ZnO Morphology Control by Pulsed Electrodeposition, The Journal of Physical Chemistry C, 117 (2012) 1502-1508.
[17] A. Serrano, O. Caballero-Calero, M.Á. García, S. Lazić, N. Carmona, G.R. Castro, M. Martín-González, J.F. Fernández, Cold sintering process of ZnO ceramics: Effect of the nanoparticle/microparticle ratio, Journal of the European Ceramic Society, (2020).
[18] D. Gallach, A. Muñoz-Noval, V. Torres-Costa, M. Manso-Silván, Luminescence and fine structure correlation in ZnO permeated porous silicon nanocomposites, Physical Chemistry Chemical Physics, 17 (2015) 20597-20604.
[19] C.V. Manzano, Alegre. D, O. Caballero-Calero, B. Alén, M. S. Martín-González, Synthesis and luminescence properties of electrodeposited ZnO films, Journal Applied Physics, 100 (2011) 043538.
[20] C.V. Manzano, G. Bürki, L. Pethö, J. Michler, L. Philippe, Determining the diffusion mechanism for high aspect ratio ZnO nanowires electrodeposited into anodic aluminum oxide, Journal of Materials Chemistry C, 5 (2017) 1706-1713.
[21] M. Newville, B. Ravel, D. Haskel, J.J. Rehr, E.A. Stern, Y. Yacoby, Analysis of multiple-scattering XAFS data using theoretical standards, Physica B: Condensed Matter, 208-209 (1995) 154-156.
[22] G.B. Harris, Quantitative Measurement of Preferred Orientation in Rolled Uranium Bars, Philosophical Magazine, 43 (1952) 113-123.
[23] J. Haug, A. Chassé, M. Dubiel, C. Eisenschmidt, M. Khalid, P. Esquinazi, Characterization of lattice defects by x-ray absorption spectroscopy at the Zn K-edge in ferromagnetic, pure ZnO films, Journal of Applied Physics, 110 (2011) -.
[24] R. Revel, D. Bazin, A.-M. Flank, Influence of cations vacancies on the K and LIII Zn edges of spinel-related compounds, Journal of Synchrotron Radiation, 6 (1999) 717-718.
[25] A. Kuzmin, S. Larcheri, F. Rocca, Zn K-edge XANES in nanocrystalline ZnO, Journal of Physics: Conference Series, 93 (2007) 012045.
[26] G.D. Mahan, Intrinsic defects in ZnO varistors, Journal of Applied Physics, 54 (1983) 3825-3832.
[27] J. Rubio-Zuazo, A. Chainani, M. Taguchi, D. Malterre, A. Serrano, G.R. Castro, Electronic structure of FeO, ɣ-Fe_2O_3 and Fe_3O_4 epitaxial films using high-energy spectroscopies, Physical Review B, 97 (2018) 235148.
[28] M. Abuín, A. Serrano, J. Chaboy, M.A. García, N. Carmona, XAS study of Mn, Fe and Cu as indicators of historical glass decay, Journal of Analytical Atomic Spectrometry, 28 (2013) 1118-1124.
[29] B. Ravel, M. Newville, ATHENA, ARTEMIS, HEPHAESTUS: data analysis for X-ray absorption spectroscopy using IFEFFIT, Journal of Synchrotron Radiation, 12 (2005) 537-541.
[30] S.C. Abrahams, J.L. Bernstein, Remeasurement of the structure of hexagonal ZnO, Acta Crystallographica Section B, 25 (1969) 1233-1236.

Supporting information

Crystal Defects and Optical Emissions of

Pulse Electrodeposited ZnO Films

Cristina V. Manzano[1,*], Aida Serrano[2], Álvaro Muñoz-Noval[3],
José F. Fernandez[2] and Marisol Martín-González[1,*]

Table S1. Harris texture coefficient, standard deviation, FWHM, and crystalline size for the different ZnO films obtained from the XRD measurements.

Reduction potential	Peak (*hkl*)	Intensity XRD	Intensity JCPDS	Texture coefficient ($TC_{(hkl)}$)	Standard deviation (σ)	FWHM (002)	Crystallite size (nm)
-1.5 V	100	6	569	0.20	1.49	0.13	62.7
	002	84	415	**3.99**			
	101	8	999	0.16			
	110	3	308	0.19			
	103	6	265	0.45			
-1.3 V	100	16	569	0.01	1.95	0.15	57.1
	002	4461	415	**4.91**			
	101	38	999	0.02			
	110	7	308	0.01			
	103	27	265	0.05			
-0.9 V	100	18	569	0.03	1.94	0.14	61.8
	002	2416	415	**4.88**			
	101	34	999	0.03			
	110	14	308	0.04			
	103	10	265	0.03			
-0.6 V	100	0	569	0	2.00	0.15	55.4
	002	3428	415	**5.00**			
	101	0	999	0			
	110	0	308	0			
	103	0	265	0			